ACSNANO

www.acsnano.org

ARTICLE

# Azo-Branched Covalent Organic Framework Thin Films as Active Separators for Superior Sodium–Sulfur Batteries

Congcong Yin, Zhen Li, Decheng Zhao, Jingying Yang,* Yi Zhang, Ya Du, and Yong Wang*

Cite This: *ACS Nano* 2022, 16, 14178–14187

Read Online

ACCESS | Metrics & More | Article Recommendations | Supporting Information

**ABSTRACT:** **Sodium–Sulfur (Na–S) batteries are outstanding for their ultrahigh capacity, energy density, and low cost, but they suffer from rapid cell capacity decay and short lifespan because of serious polysulfide shuttle and sluggish redox kinetics. Herein, we synthesize thin films of covalent organic frameworks (COFs) with azobenzene side groups branched to the pore walls. The azobenzene branches deliver dual functions: (1) narrow the pore size to the sub-nanometer scale thus inhibiting the polysulfide shuttle effect and (2) act as ion-hopping sites thus promoting the $Na^+$ migration. Consequently, the Na–S battery using the COF thin film as the separator exhibits a high capacity of 1295 mA h $g^{-1}$ at 0.2 C and an extremely low attenuation rate of 0.036% per cycle over 1000 cycles at 1 C. This work highlights the importance of separator design in upgrading Na–S batteries and demonstrates the possibility of functionalizable framework materials in developing high-performance energy storage systems.**

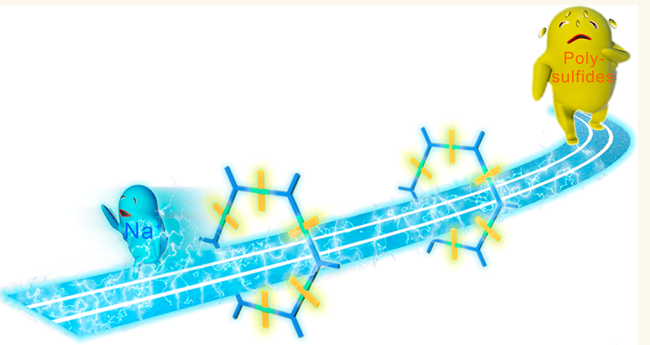


**KEYWORDS:** *azobenzene, battery separators, covalent organic frameworks (COFs), polysulfide shuttle effect, sodium–sulfur batteries*

## INTRODUCTION

Sodium–Sulfur (Na–S) batteries are distinguished among secondary batteries for their ultrahigh theoretical specific capacity (1675 mA h $g^{-1}$) of sulfur cathodes and superior energy density (1274 W h $kg^{-1}$) as well as the overwhelming advantages of low cost and environmental friendliness.[1−4] However, deploying Na–S batteries in real-world applications is plagued by obstacles that weaken their performance. Predominantly, the high reactivity of easily soluble sodium polysulfide and shuttle effect in liquid electrolyte result in fast capacity fading, sluggish kinetics, and low Coulombic efficiency.[5,6]

As a critical component in Na–S batteries, the separator serves as an insulator between electrodes and allows the flow of cations.[7,8] The ionic transport behaviors and electrochemical performances are significantly affected by the structure of separators.[9] Nevertheless, studies on separators in Na–S batteries are extremely rare compared to extensive research efforts on the electrodes. Usually, glass-fiber (GF) separators have been predominantly used in Na–S batteries.[10] However, GF separators possessing micrometer-sized pores allow the transport of both cations and their counterions, leading to rapid decline of capacity during cycling usages. In response to this issue, functional barrier layers have been built on the macroporous supports, thus restraining the polysulfide migration.[11,12] The barrier layers containing much smaller pores function as the separator to effectively inhibit the polysulfide shuttle.[13,14] Unfortunately, the introduction of a much denser barrier layer on the macroporous support inevitably brings about undesired impedance for sodium ion ($Na^+$) transport because of the permeability-selectivity trade-off.[15] Even worse, the retarded $Na^+$ diffusion depresses the reactivation of $Na_2S$, decreasing reaction kinetics and specific capacity. Therefore, desire is high for selective separators capable of blocking the passage of polysulfide at no expense of the transport of sodium ions.

Covalent organic frameworks (COFs) featuring intrinsic nanopores and structural tunability have flourished as a new class of crystalline polymers.[16−20] With designable pore chemistry and structure via chemical assembly of molecular

Received: May 2, 2022
Accepted: August 18, 2022
Published: August 22, 2022







https://doi.org/10.1021/acsnano.2c04273
*ACS Nano* 2022, 16, 14178–14187

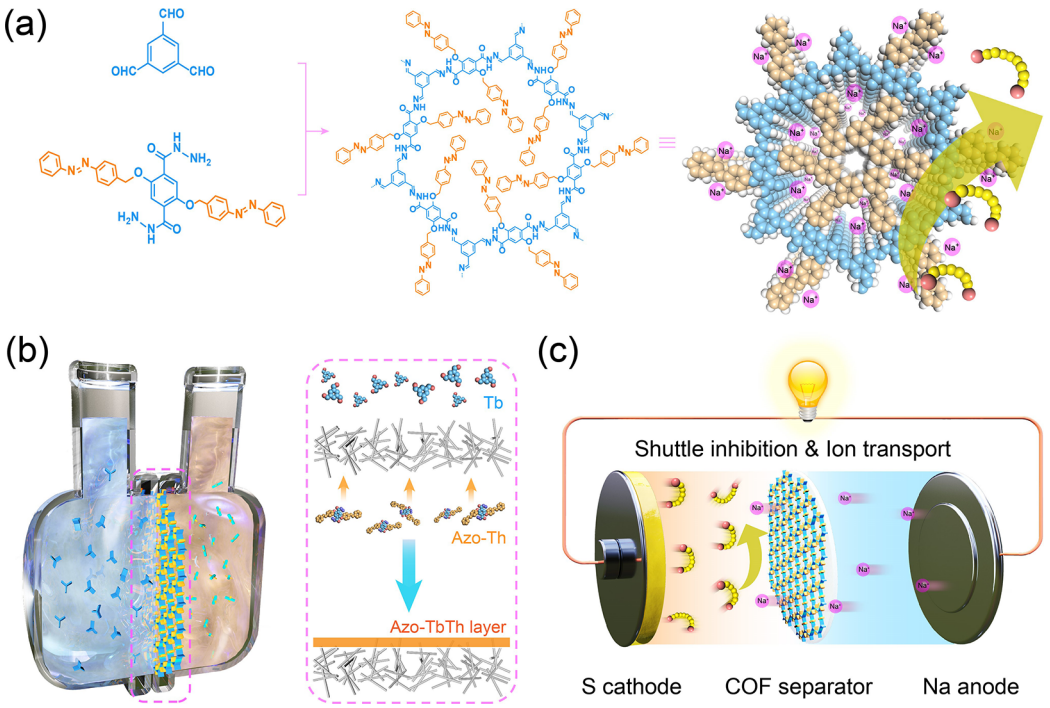


**Figure 1. Schematic illustration of the synthesis and usage of COF thin films as the separators of Na−S batteries. (a) Synthetic scheme of the azobenzene-branched COFs and their function of blocking polysulfide and selective transport of $Na^+$. (b) Synthetic illustration of the interfacial polymerization of COF thin films. (c) Schematic diagram of the Na−S battery with COF separators allowing the fast $Na^+$ transport and blocking polysulfide.**

building units, COFs exhibit great potential in energy storage.[21−23] Moreover, the strong covalent bonds in COFs afford robust scaffoldings to survive harsh operating conditions,[24] which may ensure cyclic stability and a long lifespan. Very recently, COFs have been used to improve the performance of Li ion batteries and Li−S batteries. For instance, the pore size of COFs was elaborately designed to block polysulfide in Li−S batteries.[25,26] Unfortunately, because of the barrier effect of the COF layer, the Li ion transport rate as well as the specific capacity was reduced.

Considering the designable pore size and chemistry as well as the structural robustness of COFs, we envision that meticulously designed COFs in the form of thin films may work as active separators to upgrade the performance of Na−S batteries. A critical point in the design of such COFs is to find a way to facilitate the transport of sodium ions through the narrow intrinsic pores in COFs. Previously, redox-active sites were introduced in molecular structures of COFs for elevating ion transport and specific capacity of Li−S batteries.[27−31] However, these redox-active sites were fixed in the skeleton of COFs, and a large number of the redox sites was shaded in the rigid skeleton, leading to poor accessibility and utilization.

Herein, we demonstrate a de novo design of a COF separator for Na−S batteries. Hydrazide monomers branched with azobenzene side groups are reacted with aldehydes to afford COF thin films with narrowed pores lined with azo groups (Figure 1a). Azobenzene groups serving as redox centers can reversibly interact with $Na^+$, promoting the reversible $Na^+$ insertion and extraction during charge and discharge cycles.[31−33] Besides, the lone pair electrons of nitrogen are prone to coordinate with $Na^+$, further facilitating the $Na^+$ migration through reversible coordination bonds. Via interfacial polymerization (Figure 1b), a continuous COF thin layer with a thickness of ∼70 nm is formed on the macroporous substrate, and the COF thin layer possesses superior mechanical stability and excellent interfacial functionality. On the one hand, the azobenzene side groups narrow the pore diameter to the sub-nanometer scale and thus effectively block the polysulfide shuttle. On the other hand, they establish ion-hopping sites on the directionally aligned nanochannels and consequently facilitate the migration of $Na^+$ by lowering the transport resistance (Figure 1c). Thanks to the synergetic effect of the azo groups branched to the COF pore walls, such a COF thin film blocks polysulfide while accelerating the $Na^+$ transport, and the Na−S battery using this COF thin layer as the separator shows significantly enhanced specific capacity, rate performance, and ultralow attenuation rate of 0.036% per cycle over 1000 cycles.

## RESULTS AND DISCUSSION

The azobenzene-branched COFs were synthesized under solvothermal conditions by the condensation of 1,3,5-triformylbenzene (Tb) with azobenzene-modified hydrazide linkers (Azo-Th), which is denoted as Azo-TbTh. The chemical structure of Azo-TbTh was confirmed by Fourier transform infrared (FT-IR) and solid-state $^{13}C$ NMR spectra (Figures S1 & S2). Compared with the corresponding aldehyde and azobenzene monomers, the characteristic signal of C═N (1660 $cm^{-1}$) appears in the Azo-TbTh skeletons. Meanwhile, the stretching vibration peaks of C═O (1697 $cm^{-1}$) and N−H (3326 and 3415 $cm^{-1}$) from Tb and Azo-Th are attenuated. The $^{13}C$ NMR spectrum is further evidence of the formation of hydrazone linkages, by giving a typical peak at 152 ppm assigned to hydrazone carbon. In addition, the characteristic peaks at 179 and 185 ppm are ascribed to azobenzenyl and phenyl carbons connected with amide units, respectively.


https://doi.org/10.1021/acsnano.2c04273
ACS Nano 2022, 16, 14178−14187

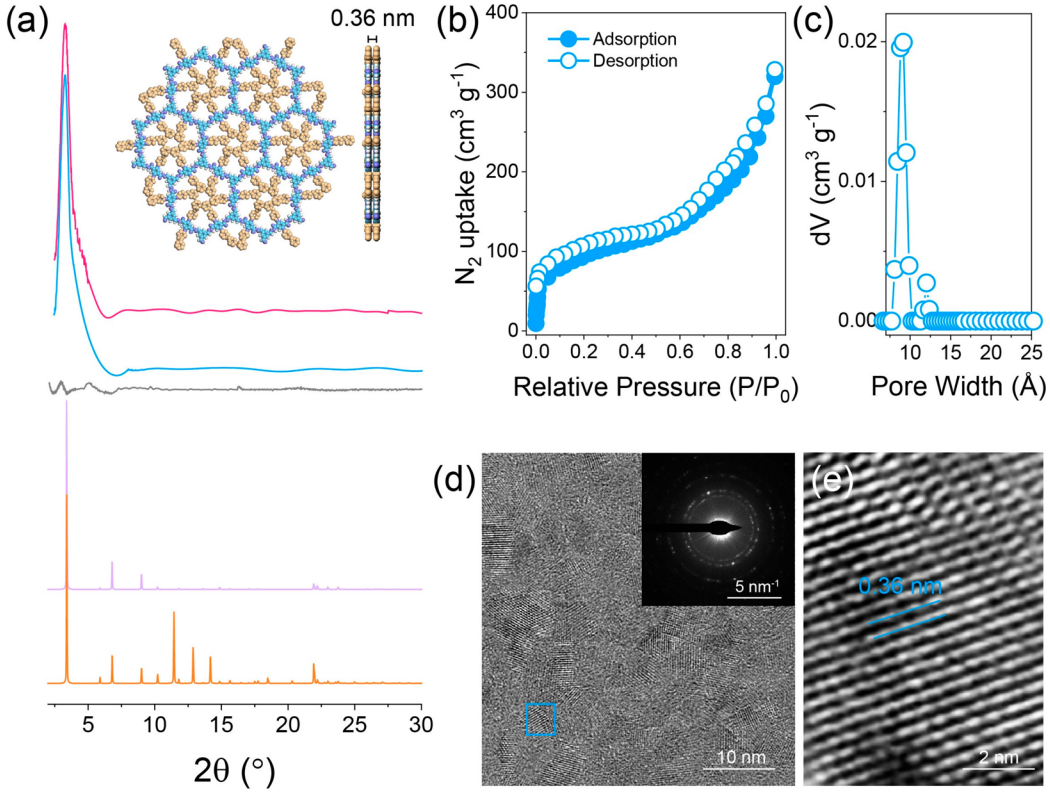


**Figure 2. Structure characterizations of Azo-TbTh. (a) Comparison of the PXRD patterns of Azo-TbTh (red curve), the Pawley refinement result (blue curve) and their difference (black curve), the simulated patterns for eclipsed (purple curve) and staggered (orange curve) stacking modes. (insets) The top and side views of Azo-TbTh in the eclipsed stacking mode. (b) $N_2$ adsorption and desorption isotherms and (c) the pore size distribution of Azo-TbTh. (d) HRTEM image of Azo-TbTh. (inset) SAED pattern. (e) Enlarged TEM image of the boxed area in (d).**

Powder X-ray diffraction (PXRD) indicated the formation of the desired crystalline framework. As illustrated in Figure 2a, the diffraction pattern of Azo-TbTh reveals an intense peak at 3.33° and a minor peak at 26.55°, affiliating to (100) and (001) facets, respectively. The lattice modeling and Pawley refinement of Azo-TbTh were simulated using Materials Studio, which reveals the probable structure in the eclipsed and staggered stacking modes. After geometry optimization of the ideal models, Azo-TbTh assumes $P_3$ space group with optimized unit cell parameters of $a = b = 30.53$ Å, $c = 3.66$ Å, $\alpha = \beta = 90.00°$, and $\gamma = 120.00°$. In addition, Pawley refinement based on the optimized eclipsed mode revealed a good match with the experimental result ($R_p$ = 3.87% and $R_{wp}$ = 5.06%). The $N_2$ adsorption−desorption isotherm curves recorded at 77 K revealed the highly porous nature of Azo-TbTh (Figure 2b). The adsorption isotherm curve exhibits a sharp rise in the relative pressure range below 0.05, which can be determined as a type I sorption isotherm, indicating its microporous structure. The Brunauer−Emmett−Teller (BET) surface area was estimated to be 528 $m^2 g^{-1}$ from the adsorption data in the range of $P/P_0$ from 0.002 to 0.05 (Figure S3). The pore size distribution analysis was calculated based on the nonlocal density functional theory (NLDFT) cylindrical pore model (Figure 2c). The result shows a prominent distribution profile centered at 0.91 nm, in agreement with the calculated pore (0.83 nm) size for the eclipsed stacking mode. This aperture is much smaller than that of the COFs without branched azobenzene groups, which is 2.8 nm.[34] Importantly, the angstrom-sized nanochannels are tight enough to block polysulfide (Table S1),[12] endowing Na−S batteries with good cyclic performance and long lifespans. The crystalline nature of Azo-TbTh was confirmed by high-resolution transmission electron microscopy (HRTEM) and selected area electron diffraction (SAED) (Figure 2d,e). Clearly, the distinct lattice fringes indicate the *d*-spacing value of Azo-TbTh is 0.36 nm, which matches well with that obtained from the PXRD pattern. The thermal stability of Azo-TbTh was confirmed by thermogravimetric analysis (TGA), which exhibits no weight loss up to 330 °C (Figure S4). This high stability ensures structural integrity of Azo-TbTh in the cyclic operation of charge−discharge processes. Based on the above results, we can conclude that the azobenzene-branched COFs are successfully synthesized, and the high porosity and excellent thermal stability are highly desired for the separators of Na−S batteries.

The Azo-TbTh thin films were synthesized by interfacial polymerization on a commercial glass-fiber support (Figures 1b, S5, & S6). Over the course of 5 d, a yellow film formed on the surface of the GF support facing the organic phase. The hydrazone structures of the resulting the Azo-TbTh separator were verified by attenuated total reflection infrared (ATR-IR) spectra (Figure S7). The crystalline structure of the Azo-TbTh film was examined using HRTEM and grazing incidence wide-angle X-ray scattering (GIWAXS) (Figures S8 & S9). Distinct lattice fringes are obtained, and the sharp diffraction spots are also observed in the SAED pattern, evidencing the high structural ordering of the Azo-TbTh film. Moreover, the diffraction ring of 3.9 $nm^{-1}$ represents the (100) plane of the


https://doi.org/10.1021/acsnano.2c04273
ACS Nano 2022, 16, 14178−14187

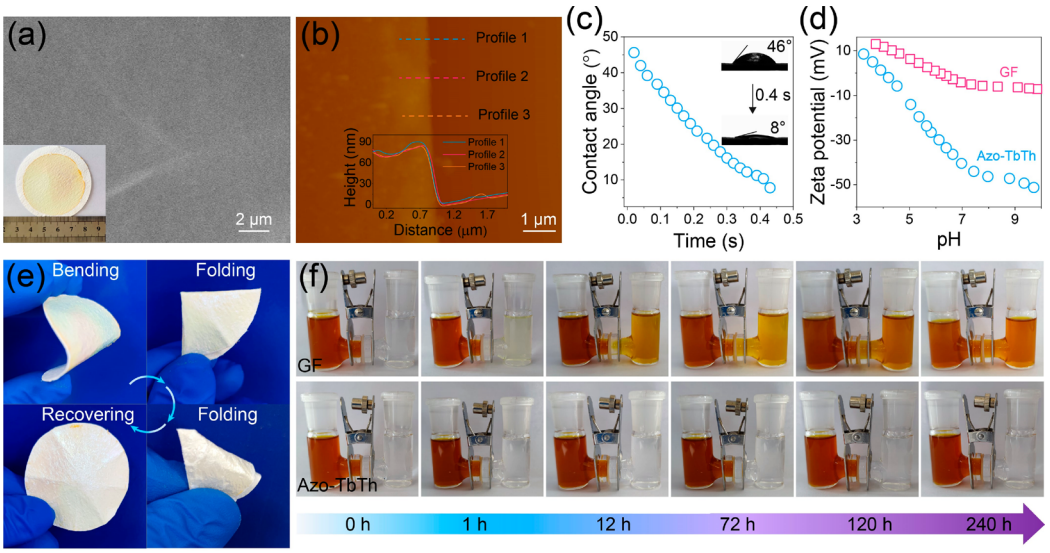


**Figure 3. Microstructures and properties of the Azo-TbTh separator and the bare GF separator. (a) The surface SEM image of the Azo-TbTh separator. (inset) Digital photo of the Azo-TbTh separator. (b) The AFM image of the Azo-TbTh layer. (inset) Corresponding height profile. (c) The change of the contact angle of the electrolyte on the Azo-TbTh separator with time. (d) Zeta potentials. (e) Photographs showing the flexibility of the Azo-TbTh separator. (f) Photographs demonstrating the permeation of polysulfide through the bare GF separator and the Azo-TbTh separator.**

Azo-TbTh, which matches well with the PXRD result. Digital image and scanning electron microscopy (SEM) observation reveal a continuous, smooth, and crack-free film that contour the underlying GF support, indicative of the ultrathin thickness of the film (Figure 3a). The Azo-TbTh separator has a thickness of 70 nm, which was determined by atomic force microscopy (AFM) (Figure 3b) and double-checked by a cross-sectional SEM image (Figure S10). This ultrathin film formed on the macroporous support is expected to effectively block the passage of polysulfide without adding extra resistance to ion transport, thus improving the specific capacity of the battery.

During the operation of the Na−S batteries, the wettability of the electrolyte to separators has an important influence on its electrochemical performance.[35] As shown in Figure 3c, the electrolyte is completely absorbed by the Azo-TbTh layer, with the dynamic contact angle rapidly declining to 8° in 0.4 s. This is mainly ascribed to the strong affinity between negatively charged Azo-TbTh films and polar molecules in electrolyte. The surface charging property was further investigated by a surface zeta potential test. As shown in Figure 3d, the Azo-TbTh separator (supported on GF) exhibits a strong negative value of −36 mV, while the bare GF support presents an inferior value of −5 mV. The increased negative charging of the Azo-TbTh separator should be attributed to the electron-donating nature of the hydrazone groups,[36] which also contributes to block polysulfide (also negatively charged) because of electrostatic repulsion.

For practical applications, the separator with favorable mechanical properties is also important.[37,38] In this regard, we performed a series of flexibility tests by bending the separators to different extents. Notably, the tests with the curvatures from 167 to 333 $m^{-1}$ produce no visible fragmentation, cracks, or detachment of the Azo-TbTh layer (Figures S11 & S12). After we increased the bending curvature to 400 $cm^{-1}$, cracks were observed from SEM images, but the Azo-TbTh layer is still strongly connected to the GF substrate. In addition, the integrity of the Azo-TbTh separator is kept intact even after being folded and recovered in quarters, further suggesting its superior flexibility and foldability (Figure 3e). In light of the above results, we visually elucidated the operation and impediment ability toward the crossover of soluble polysulfide (Figures 3f & S13). The permeation tests were conducted in a U-shaped cell and analyzed using UV−vis spectra. About 5% of polysulfides permeate through the bare GF separator within 1 h, implying an inferior polysulfide blocking capacity. In sharp contrast, only 3% of polysulfides migrate through the Azo-TbTh separator even after 240 h, demonstrating the enhanced blocking performance of the Azo-TbTh separator toward soluble polysulfides. This superiority is attributed to the synergistic effect of the barrier function of the narrow pore sizes and the electrostatic repulsion of the enhanced negative charging.

To further elucidate the effects of the Azo-TbTh separator on the $Na^+$ transport behavior, the ionic conductivity and $Na^+$ transference number were evaluated. Surprisingly, as shown in Figure 4a, the ionic conductivity of the symmetric cell with the Azo-TbTh separator (6.9 mS $cm^{-1}$) is much higher than that of the bare GF separator (3.9 mS $cm^{-1}$), indicating the high $Na^+$ conductive capacity of the Azo-TbTh separator. Besides, the Azo-TbTh separator shows a superior $Na^+$ transference number of 0.89 (Figure 4b). Usually, the compact coating layer tends to block the diffusion way and decrease sodium ion conductivity. Interestingly, our microporous Azo-TbTh separator shows a much better ionic migration than the macroporous GF support. This should be attributed to the azobenzene groups branched to the COF pores as "handrails" accelerating the transport of sodium ions. Moreover, electronegative Azo-TbTh promotes wettability of the electrolyte to the separator, facilitating ion pair dissociation and mobility of $Na^+$.[39] Thin films of another COF, ACOF-1, having a similar framework structure as well as a closing pore size (~9.5 Å) to Azo-TbTh but without azobenzene groups, was synthesized on the GF support using the same interfacial polymerization process (Figures S14−S16).[40] Their separator properties were tested and compared with the Azo-TbTh separator, thus


https://doi.org/10.1021/acsnano.2c04273
ACS Nano 2022, 16, 14178−14187

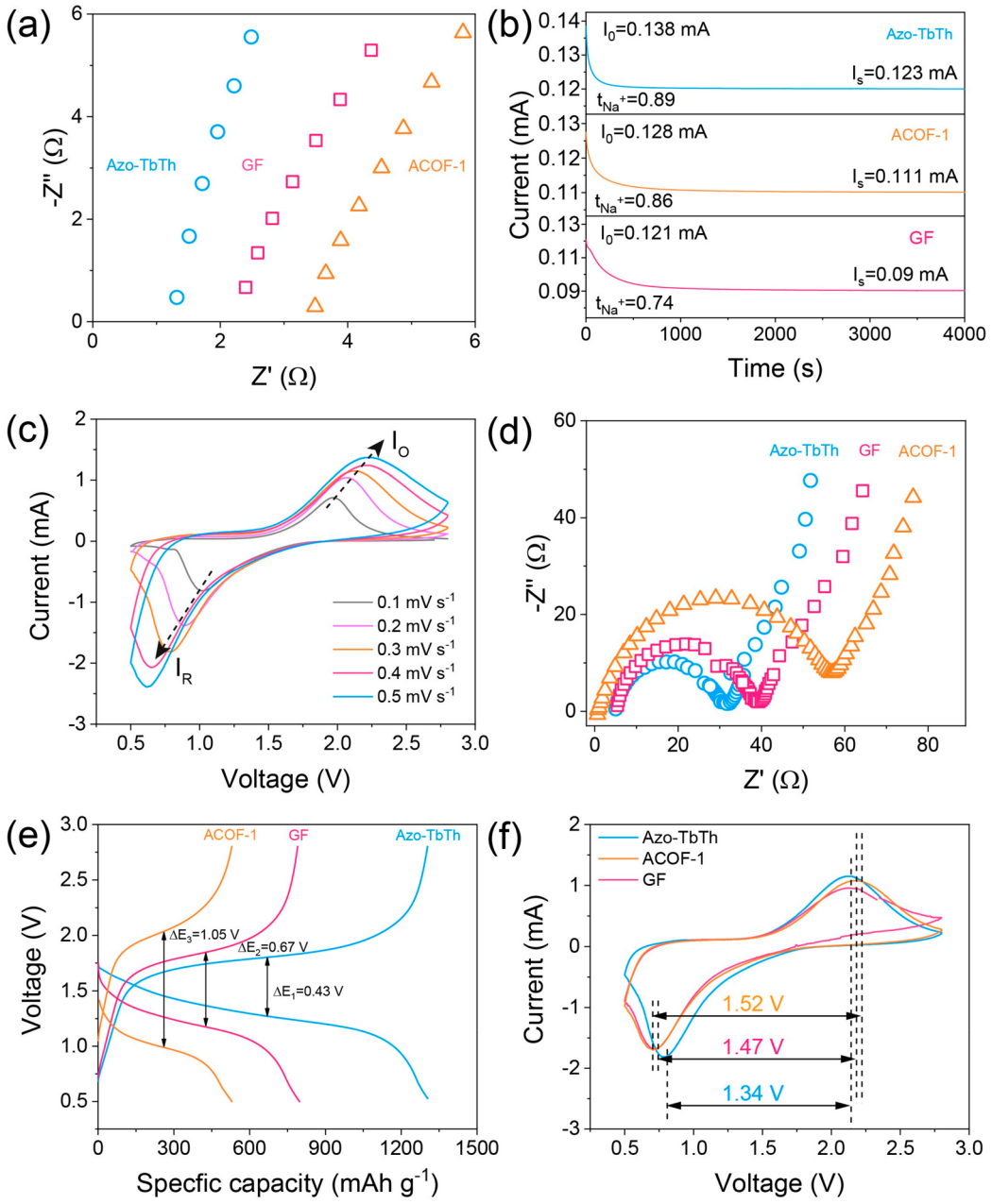


**Figure 4. Ion conductivity behaviors of batteries with various separators. (a) Impedance plots and (b) chronoamperometric curves. (c) CV profiles at different scan rates of the battery with the Azo-TbTh separator. (d) EIS and (e) the charge−discharge voltage profiles at 0.2 C. (f) CV comparison at the scan rate of 0.1 mV $s^{-1}$.**

illustrating the critical role of the azobenzene branches. As clearly shown in Figure 4d, the $Na^+$ transference number of the ACOF-1 separator has an obvious reduction because of the absence of conductive sites. As a result, the introduction of compact ACOF-1 layer inevitably increases the ionic transport resistance.

The electrochemical performance of Na−S batteries at various scan rates (0.1−0.5 mV $s^{-1}$) was investigated to explore the kinetic behavior and $Na^+$ diffusion properties. The discharge/charge behavior was investigated using cyclic voltammetry (CV) over the extended range of 0.5−2.8 V. From the CV curves in Figures 4c and S17, the anodic and cathodic scans present apparent oxidation peaks ($I_O$) and reduction peaks ($I_R$), respectively. The tendency of peak current variation is in good agreement with that of the scan rates changes, validating their highly relevant relationship from linear fitting results (Figure S18). Typically, the $Na^+$ diffusion coefficient ($D_{Na^+}$) of $I_R$ for the battery equipped with the Azo-TbTh separator is 3.4 and 1.4 times higher than those of the battery using bare GF and ACOF-1 as the separator, respectively, reflecting the outstanding ionic diffusion rate of the Azo-TbTh separator. Electrochemical impedance spectra (EIS) were recorded to further investigate the interfacial resistance (Figure 4d). It is found that the battery with the Azo-TbTh separator experiences the lowest charge transfer resistance and internal resistance. The slope of the fitting line corresponding to $D_{Na^+}$ positively reflects the mobility of $Na^+$ within the electrode. Obviously, the battery with the Azo-TbTh separator exhibits the highest $D_{Na^+}$, evidencing the importance of separator design in promoting $Na^+$ diffusion.


https://doi.org/10.1021/acsnano.2c04273
ACS Nano 2022, 16, 14178−14187

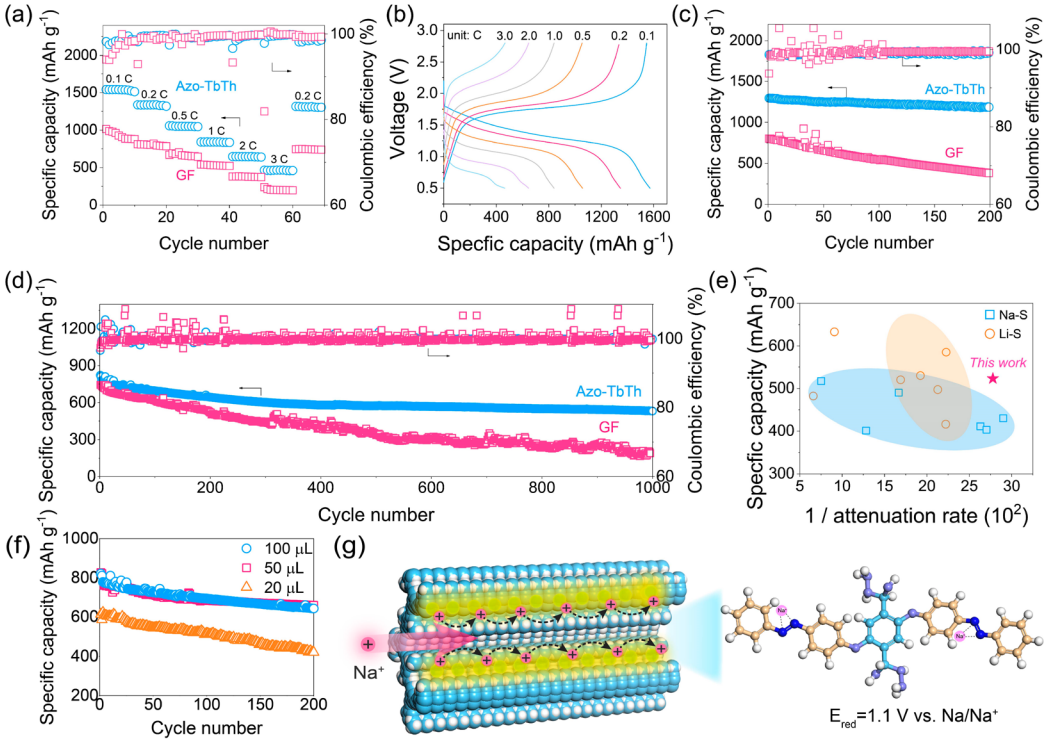


**Figure 5. Battery performances. (a) Rate performances of the Azo-TbTh and GF-equipped batteries. (b) Charge/discharge voltage profiles of the Azo-TbTh-equipped battery. (c) Discharge−Charge capacity and Coulombic efficiency of Azo-TbTh and GF equipped batteries at 0.2 C. (d) Cycle performance of Azo-TbTh and GF-equipped batteries up to 1000 cycles at 1 C. (e) Stability performance comparison between our Azo-TbTh-equipped battery and other Na−S and Li−S batteries reported in the literature. (f) Cycle performance for Azo-TbTh-equipped batteries of different electrolyte amounts at 1 C. (g) Mechanism understandings on the fast $Na^+$ migration within the Azo-TbTh separator.**

Notably, all cathodic and anodic scans only show one peak; this is mainly attributed to the micropore confinement effect,[41] indicating the direct conversion between S and $Na_2S$ (Figure S19). With the discharging-charging going on at 1 C, inactive sulfur-related species gradually agglomerate and deposit in the microporous lychee-derived carbon cathode, leading to the increased interfacial resistance (Figure S20). Besides, two cathode peaks are observed after the cathodes are operated for 100 cycles, suggesting the reversible transitions between S and $S_{4-8}$ (Figure S21).

The discharge/charge curves of various separators at 0.2 C were further evaluated. Two voltage plateaus in the discharge curves match well with the CV profiles (Figures 4c,e & S17). The Na−S battery with the Azo-TbTh separator shows the highest peak intensity, largest enclosed area, and narrowest potential difference among these three samples, which states its electrochemical activity and Na-polysulfide reaction kinetics. Besides, from the CV curves at the scan rate of 0.3 mV $s^{-1}$ (Figure 4f), the Azo-TbTh-based battery presents the narrowest polarization voltage (1.34 V) compared to batteries using GF and ACOF-1 as the separator, further demonstrating the superior kinetics of redox conversion reactions.

The rate capabilities of the Azo-TbTh and bare GF separator were investigated at various current densities from 0.1 to 3 C (Figure 5a). The discharge capacities of Azo-TbTh based battery were determined to be 1540, 1336, 1057, 840, 646, and 465 mA h $g^{-1}$ at 0.1, 0.2, 0.5, 1, 2, and 3 C, respectively, validating good rate performance and specific capacity. When the current density is adjusted from 3 to 0.2 C, the discharge capacity can recover back to 1314 mA h $g^{-1}$, implying an outstanding stability at various rates. On the contrary, inferior discharge capacity and rate performance of the GF separator are observed under the same condition. It is notable that the discharge capacity of the battery with the GF separator declines from 1013 down to 880 mA h $g^{-1}$ after 10 cycles at 0.1 C as a result of the rapid consumption of intermediate polysulfide through the separator with micrometer-sized pores. The corresponding galvanostatic discharge/charge curves of these batteries at different current density are depicted in Figures 5b and S22. It is shown that the Azo-TbTh battery exhibits the better ability for inhibition of polarization. These results further confirm that the Azo-TbTh separator functions as a barrier layer for polysulfide and as a promoter for sodium ions, thus boosting the performance of Na−S batteries.

Figures 5c and S23 explored the cyclic performance of Na−S batteries with Azo-TbTh and GF as the separators at 0.2 C. Benefiting from the conspicuous ability to block polysulfide and enhanced charge conductivity of Azo-TbTh, the Azo-TbTh-based battery delivers an initial average discharge capacity of 1278 mA h $g^{-1}$ and an average decay to 91.8% capacity retention after 200 cycles is obtained, corresponding to an average 0.042% attenuation per cycle. Besides, 99.1% of their average Coulombic efficiency is retained. In contrast, the GF-based battery shows an initial discharge capacity of 802 mA h $g^{-1}$ and drops to 545 mA h $g^{-1}$ after 100 cycles. The attenuation per cycle rises to 0.32%, reflecting a severe polysulfide shuttle effect. To further investigate the long-term cycling stability at a higher current rate, the Azo-TbTh-based batteries were tested at 1 C for 1000 cycles (Figures 5d & S24). They initially deliver a high average capacity of 820 mA h $g^{-1}$ and maintain a decent average capacity of 524 mA h $g^{-1}$ after 1000 cycles, implying an extremely low average


https://doi.org/10.1021/acsnano.2c04273
ACS Nano 2022, 16, 14178−14187

attenuation rate of 0.036% per cycle and a considerable average Coulombic efficiency of 99.3%. Moreover, the Azo-TbTh-based battery still exhibits a favorable cycling stability, even at a higher current density of 3 C (Figure S25). In contrast, the GF-based battery shows an initial discharge capacity of 744 mA h $g^{-1}$, and the capacity is only maintained at 189 mA h $g^{-1}$ after 1000 cycles at a current density of 1 C. For the purpose of achieving high-energy-density Na−S batteries, the sulfur contents of the S/carbon cathode were increased to 60 and 70 wt %, accompanied with the areal sulfur loading of 1.5 mg $cm^{-2}$. As shown in Figure S26, the Azo-TbTh-equipped cells with sulfur contents of 60 and 70 wt % exhibit initial discharge capacities of 304 and 152 mA h $g^{-1}$ and maintain 236 and 97 mA h $g^{-1}$ after 200 cycles at 0.2 C, corresponding to 0.22% and 0.36% attenuations per cycle. We note that these performances are weaker than that of the cell with sulfur content of 40 wt %, and such an inferior electrochemical performance at higher sulfur content has been frequently observed in Na−S batteries.[1,42] The decreased capacity is attributed to the pore volume of lychee-derived carbon cathode, which is calculated to be 0.374 $cm^3$ $g^{-1}$ and can only accommodate about 43 wt % sulfur (Figure S19). Extra sulfur would proceed through the pore space, leading to a serious polysulfide formation and dissolution during charge/discharge processes. Nevertheless, the decent attenuation rates with high sulfur content demonstrate that the Azo-TbTh separator is an ideal polysulfide barrier for Na−S batteries. In order to practically analyze the effect of the separator on the sodium anode, the batteries were disassembled after running for 1000 cycles. From Figure S27, it can be clearly observed that much bulk polysulfide attached on the surface of anode for the GF-based battery, and the corresponding sulfur content is determined to be 11.8 wt %. However, the Azo-TbTh-based battery possesses a smooth and intact anode surface and a low sulfur content down to 0.4 wt %.

Note that the Azo-TbTh separators exhibit highly efficient trapping of polysulfide combined with fast ion transition. We compared the attenuation rate and ultimate capacity at 1 C of our Na−S batteries using Azo-TbTh as the separator with other previously reported Na−S and Li−S batteries. As depicted in Figure 5e and Table S2, our Azo-TbTh-based battery exhibits the highest comprehensive performance among state-of-the-art Na−S batteries. Importantly, the Azo-TbTh-based battery developed in this work shows good attenuation rate, and the ultimate specific capacity is ∼2 times higher than most of the other Na−S batteries. Moreover, the Azo-TbTh-equipped batteries also display creditable durability toward current Li−S batteries, demonstrating the superiority of azo compounds in alkali-based batteries.

The amount of electrolyte is critical for the energy density of batteries because electrolyte may contribute significantly to the total battery weight.[43] To evaluate the cycle performances with lower electrolyte amounts, Azo-TbTh-equipped cells were assembled with electrolyte amounts of 20 and 50 $\mu$L and tested at 1 C (Figure 5f). The battery with 50 $\mu$L of electrolyte delivers a similar electrochemical performance to that with 100 $\mu$L. Meanwhile, the battery capacity is moderately decayed with 20 $\mu$L of electrolyte, which should be attributed to the inadequate filling of the electrolyte into the relatively thick GF substrate and consequently hampered conduction of $Na^+$.[5,43] However, even for the cell with 20 $\mu$L of electrolyte, its specific capacity is still superior to most of the reported Na−S batteries (Table S2). Therefore, the Azo-TbTh-based battery can effectively operate with lean electrolyte, which is highly desired for high-energy-density Na−S batteries.

The fast $Na^+$ migration through the Azo-ThTb separator should be ascribed to the favorable interaction between azo groups and metal ions.[32,33] As shown in Figures 5g and S28, such an interaction may be described in the following two ways. (1) The azo groups serve as redox-active sites for sodium intercalation/deintercalation. The reduction potential of the azo fragment was determined using density functional theory (DFT) calculations (Figure 5g). With the electrons provided from dissolved polysulfides, the Azo-Th displays a reduction potential of 1.1 V versus $Na/Na^+$ for the reduced N−N fragment. Besides, the Gibbs free energy of the interaction process is calculated to be −104.6 kJ $mol^{-1}$, ensuring its thermodynamic feasibility. (2) Azo-containing ligands have been previously reported to have the capability to coordinate with metal ion centers.[44] In the present work, the lone pair electrons of nitrogen are expected to coordinate with $Na^+$, enabling the migration of $Na^+$ through reversible coordination bonds. These $Na^+$-active sites provided by the directionally aligned azo groups serve as the efficient $Na^+$ hopping path, which would accelerate the diffusion of $Na^+$ by lowering the diffusion barrier.

The $Na^+$ transport sites provided by branched azo groups are also important for ion selectivity and favorable ion conductivity.[15,45] Compared with the GF separator, the ACOF-1 separator without azo groups shows a moderate ion selectivity and a significantly reduced ion diffusion rate. Even the Azo-ThTb separator has a similar pore size of ∼0.91 nm; it exhibits the best ion selectivity and conductivity in the three separators. These can be evidenced by the experimental results of the comparison of $Na^+$ transference number and migration resistance between three separators (Figure 4a,b). Obviously, the Azo-TbTh separator exhibits the smallest resistance (1.3 Ω), the highest $Na^+$ transference number (0.89), and the largest ion conductivity (6.9 mS $cm^{-1}$), indicating its excellent single $Na^+$ transport property. These properties ensure the superior capability of the Azo-TbTh separator for selective $Na^+$ conduction in Na−S batteries.

## CONCLUSIONS

In summary, we design and synthesize azo-functionalized COF thin films and use them as active separators for Na−S batteries. Azobenzene side groups are branched to the wall of the intrinsic pores of COFs, narrowing the pore diameter down to the sub-nanometer scale and consequently restraining the polysulfide shuttle effect. Meanwhile, the abundant azobenzene sites along the COF pore wall serve as an ionic hopping path, greatly accelerating the migration of $Na^+$. The Na−S battery with this azo-functionalized COF separator exhibits exceptionally high capacity, rate performance, and an extremely low capacity-fading rate. This study improves the performances of Na−S batteries by simultaneously eliminating polysulfide shuttle and enhancing $Na^+$ transport and shows the great potential of functionalizable framework materials in developing next-generation energy storage systems.

## EXPERIMENTAL SECTION

**Synthesis of Azo-TbTh.** A Pyrex tube was charged with Tb (7.2 mg, 0.044 mmol), Azo-Th (41.8 mg, 0.065 mmol), 0.25 mL of dioxane, and 0.75 mL of mesitylene. The tube was immersed in an ultrasonic bath for 10 min; following this, 10 $\mu$L of $CF_3COOH$ was added. The tube was degassed via three-freeze−pump−thaw cycles


https://doi.org/10.1021/acsnano.2c04273
ACS Nano 2022, 16, 14178−14187

and flame-sealed. The reaction was heated at 120 °C for 72 h yielding a yellow solid at the bottom of the tube. The precipitate was then subjected to Soxhlet extraction with tetrahydrofuran (THF) for 24 h to remove any trapped guest molecules. The powder was collected and dried at 60 °C under vacuum overnight in an isolated yield of 82%.

**Preparation of Azo-TbTh Modified Separator.** The Azo-TbTh separation layer was fabricated via interfacial polymerization on the surface of a GF substrate. The substrate was vertically placed in the middle of a homemade diffusion cell, leading to each volume of 40 mL (Figures 1b and S5). An organic phase with Azo-Th (15 mg, 0.024 mmol) dissolved in dichloromethane (40 mL) and an aqueous phase of Tb (3 mg, 0.018 mmol) dissolved in the mixture of DOX/$CF_3COOH$/$H_2O$ (V/V/V = 1:0.02:39, 40 mL) were simultaneously added into the two parts of the diffusion cell. The reaction mixture was kept at room temperature for 5 d. The obtained separator was rinsed with dioxane and water in sequence to remove any residual monomers and $CF_3COOH$.

**Preparation of S/Carbon Cathodes.** Typically, commercial lychee seeds were mechanically grinded for 10 min to obtain a fine powder. The lychee powder was then treated with a 1 M KOH solution to create micropores. After being stirred for 24 h, the collected powder was dried at 100 °C overnight. The obtained powder was then heated at 800 °C for 3 h under a $N_2$ atmosphere with a heating rate of 5 °C $min^{-1}$. At last, 1 M hydrochloric acid solution was added to neutralize the residual KOH. The product was centrifuged and washed with $H_2O$ several times and dried at 70 °C overnight.

The S/carbon nanocomposite was prepared by mixing sublimate sulfur (40 wt %) and porous lychee-derived carbon (60 wt %) and heating at 150 °C for 12 h in a sealed tube. Subsequently, S/carbon nanocomposite (70 wt %) was mixed with conductive carbon black (20 wt %) and poly(vinylidene fluoride) (10 wt %) in *N*-methyl-2-pyrrolidone (NMP), forming a uniform slurry. The slurry was then spread onto aluminum foil, followed by drying at 75 °C for 24 h and mechanical cutting; circular cathodes were obtained. The areal mass loading of sulfur is controlled to be around 1 mg $cm^{-2}$, which is comparable to or even higher than that of previous works (Table S3).

**Characterizations.** PXRD measurements were recorded on a Rigaku Smart Lab diffractometer using Cu K$\alpha$ radiation by depositing powder on a glass substrate. The scan speed and step size were set as 1°·$min^{-1}$ and 0.02°, respectively. Surface areas and pore size distributions of Azo-TbTh were determined by $N_2$ adsorptions using a Micromeritics ASAP-2046. The samples were activated at 120 °C for 12 h under vacuum prior to the gas sorption analysis. HRTEM images were carried out on a JEOL JEM-F200 electron microscope. GIWAXS test was performed by a Hypix-6000 detector with X-ray wavelength of 1.5405 Å, the incident angle was set at 0.5°, and the distance of director to sample was 69.2 nm. FTIR patterns were collected on a Nicolet 8700 infrared spectrometer. The powders samples were prepared as KBr pellets, while the membrane samples were conducted on an attenuated total reflectance (ATR) accessory. Solid-state $^{13}C$ cross-polarization/magic-angle spinning (CP/MAS) NMR spectra were recorded on an Agilent 600 DD2 spectrometer (Agilent; magnetic field strength 14.1 T) at resonance frequency of 150.72 MHz for $^{13}C$ using the CP-MAS and a high-power $^{1}H$ decoupling. The powder samples were placed in a pencil-type zirconia rotor of 4.0 mm o.d. The spectra were obtained at a spinning speed of 10 kHz (4.2 $\mu$s 90° pulses), a 2 ms CP pulse, and a recycle delay of 3 s. The C signal of tetramethylsilane (TMS) at 0 ppm was used as the reference of $^{13}C$ chemical shift. TGA was carried out on a NETZSCH STA 449 F3 Jupiter thermal analyzer by heating the sample from 20 to 800 °C under a nitrogen atmosphere at a heating rate of 10 °C/min. SEM was carried out using a Hitachi S-4800 instrument at 3 kV and 10 mA. The samples were coated with gold before being submitted to SEM characterization. The surface element distribution was determined from energy-dispersive X-ray spectroscopy (EDS) at 15 kV and 20 mA. AFM (XE-100, Park Systems) was employed to detect the height profiles of the membranes. The Azo-TbTh separator was etched using a hydrofluoric acid solution (1 wt %) and transferred onto a silicon wafer and dried. The sample was then attached to a magnetic sample disk and scanned under tapping mode. Raster scanning was used with a resolution of 256 points per line at a scan rate of 1 Hz. XEI software was performed to process the AFM image. The thickness was determined from the height difference between the silicon wafer and the Azo-TbTh separator with a one-dimensional statistical function. The contact angle was measured by dynamic contact angle goniometer (Dropmeter A-100). The streaming potentials testing of separators was conducted on an electrokinetic analyzer (SurPASS, Anton Paar GmbH).

## ASSOCIATED CONTENT

### Supporting Information

The Supporting Information is available free of charge at https://pubs.acs.org/doi/10.1021/acsnano.2c04273.

FTIR and NMR spectra, and BET surface area plot of Azo-TbTh; diameter data of polysulfides; TGA curve of Azo-TbTh; digital photograph of the synthesis device; SEM image of the GF separator; FTIR spectra, TEM and SEM images, and GIWAXS pattern of the Azo-TbTh separator; digital photographs and SEM images of Azo-TbTh separators with different curvatures; UV−vis spectra of polysulfides solutions through separators; reaction scheme of ACOF-1; SEM images and contact angles of the ACOF-1 separator; CV and $Na^+$ diffusion coefficients of batteries with different separators; $N_2$ adsorption isotherms of the lychee-derived carbon; EIS and CV profiles of Azo-TbTh- and GF-based batteries; charge/discharge voltage profiles of GF-based batteries; cycling performances of Azo-TbTh-based batteries at different rates; effect of the separator on the polysulfide deposition; interaction mechanism for $Na^+$ migration; performance comparison of batteries with different separators (PDF)

## AUTHOR INFORMATION


### Corresponding Authors

**Yong Wang** − *State Key Laboratory of Materials-Oriented Chemical Engineering, College of Chemical Engineering, Nanjing Tech University, Nanjing 211816 Jiangsu, P. R. China*; orcid.org/0000-0002-8653-514X; Email: yongwang@njtech.edu.cn

**Jingying Yang** − *State Key Laboratory of Materials-Oriented Chemical Engineering, College of Chemical Engineering, Nanjing Tech University, Nanjing 211816 Jiangsu, P. R. China*; Email: jyyang@njtech.edu.cn

### Authors

**Congcong Yin** − *State Key Laboratory of Materials-Oriented Chemical Engineering, College of Chemical Engineering, Nanjing Tech University, Nanjing 211816 Jiangsu, P. R. China*

**Zhen Li** − *Institute of Advanced Synthesis, School of Chemistry and Molecular Engineering, Nanjing Tech University, Nanjing 211816 Jiangsu, P. R. China*

**Decheng Zhao** − *School of Energy Science and Engineering, Nanjing Tech University, Nanjing 211816 Jiangsu, P. R. China*

**Yi Zhang** − *School of Energy Science and Engineering, Nanjing Tech University, Nanjing 211816 Jiangsu, P. R. China*; orcid.org/0000-0002-1603-8623

**Ya Du** − *Institute of Advanced Synthesis, School of Chemistry and Molecular Engineering, Nanjing Tech University,*

*Nanjing 211816 Jiangsu, P. R. China;* orcid.org/0000-0001-9378-0138

Complete contact information is available at: https://pubs.acs.org/10.1021/acsnano.2c04273

### Notes

The authors declare no competing financial interest.

## ACKNOWLEDGMENTS

This work was financially supported by the National Natural Science Fund for Distinguished Young Scholars (21825803).

## REFERENCES

(1) Guo, Q.; Li, S.; Liu, X.; Lu, H.; Chang, X.; Zhang, H.; Zhu, X.; Xia, Q.; Yan, C.; Xia, H. Ultrastable sodium−sulfur batteries without polysulfides formation using slit ultramicropore carbon carrier. *Adv. Sci.* **2020**, *7*, 1903246.

(2) Yan, Z.; Xiao, J.; Lai, W.; Wang, L.; Gebert, F.; Wang, Y.; Gu, Q.; Liu, H.; Chou, S. L.; Liu, H.; Dou, S. X. Nickel sulfide nanocrystals on nitrogen-doped porous carbon nanotubes with high-efficiency electrocatalysis for room-temperature sodium-sulfur batteries. *Nat. Commun.* **2019**, *10*, 4793.

(3) Bao, W.; Shuck, C. E.; Zhang, W.; Guo, X.; Gogotsi, Y.; Wang, G. Boosting performance of Na-S batteries using sulfur-doped $Ti_3C_2T_x$ MXene nanosheets with a strong affinity to sodium polysulfides. *ACS Nano* **2019**, *13*, 11500−11509.

(4) Mou, J.; Liu, T.; Li, Y.; Zhang, W.; Li, M.; Xu, Y.; Huang, J.; Liu, M. Hierarchical porous carbon sheets for high-performance room temperature sodium−sulfur batteries: integration of nitrogen-self-doping and space confinement. *J. Mater. Chem. A* **2020**, *8*, 24590−24597.

(5) Ye, X.; Ruan, J.; Pang, Y.; Yang, J.; Liu, Y.; Huang, Y.; Zheng, S. Enabling a stable room-temperature sodium-sulfur battery cathode by building heterostructures in multichannel carbon fibers. *ACS Nano* **2021**, *15*, 5639−5648.

(6) Zhang, S.; Yao, Y.; Jiao, X.; Ma, M.; Huang, H.; Zhou, X.; Wang, L.; Bai, J.; Yu, Y. $Mo_2N$-$W_2N$ heterostructures embedded in spherical carbon superstructure as highly efficient polysulfide electrocatalysts for stable room-temperature Na-S batteries. *Adv. Mater.* **2021**, *33*, 2103846.

(7) Wei, C.; Han, Y.; Liu, H.; Gan, R.; Li, Q.; Wang, Y.; Hu, P.; Ma, C.; Shi, J. Advanced lithium−sulfur batteries enabled by a $SnS_2$-Hollow carbon nanofibers Flexible Electrocatalytic Membrane. *Carbon* **2021**, *184*, 1−11.

(8) Ni, X.; Qian, T.; Liu, X.; Xu, N.; Liu, J.; Yan, C. High lithium ion conductivity LiF/GO solid electrolyte interphase inhibiting the shuttle of lithium polysulfides in long-life Li-S batteries. *Adv. Funct. Mater.* **2018**, *28*, 1706513.

(9) Bauer, I.; Kohl, M.; Althues, H.; Kaskel, S. Shuttle suppression in room temperature sodium−sulfur batteries using ion selective polymer membranes. *Chem. Commun.* **2014**, *50*, 3208−3210.

(10) Carter, R.; Oakes, L.; Douglas, A.; Muralidharan, N.; Cohn, A. P.; Pint, C. L. A sugar-derived room-temperature sodium sulfur battery with long term cycling stability. *Nano Lett.* **2017**, *17*, 1863−1869.

(11) Dong, C.; Zhou, H.; Jin, B.; Gao, W.; Lang, X.; Li, J.; Jiang, Q. Enabling high-performance room-temperature sodium/sulfur batteries with few-layer 2H-$MoSe_2$ embellished nitrogen-doped hollow carbon spheres as polysulfide barriers. *J. Mater. Chem. A* **2021**, *9*, 3451−3463.

(12) Yu, X.; Manthiram, A. Performance enhancement and mechanistic studies of room-temperature sodium−sulfur batteries with a carbon-coated functional nafion separator and a $Na_2S$/activated carbon nanofiber cathode. *Chem. Mater.* **2016**, *28*, 896−905.

(13) Yang, T.; Guo, B.; Du, W.; Aslam, M. K.; Tao, M.; Zhong, W.; Chen, Y.; Bao, S. J.; Zhang, X.; Xu, M. Design and construction of sodium polysulfides defense system for room-temperature Na-S battery. *Adv. Sci.* **2019**, *6*, 1901557.

(14) Li, H.; Zhao, M.; Jin, B.; Wen, Z.; Liu, H. K.; Jiang, Q. Mesoporous nitrogen-doped carbon nanospheres as sulfur matrix and a novel chelate-modified separator for high-performance room-temperature Na-S batteries. *Small* **2020**, *16*, 1907464.

(15) Cao, Y.; Wu, H.; Li, G.; Liu, C.; Cao, L.; Zhang, Y.; Bao, W.; Wang, H.; Yao, Y.; Liu, S.; Pan, F.; Jiang, Z.; Sun, J. Ion selective covalent organic framework enabling enhanced electrochemical performance of lithium-sulfur batteries. *Nano Lett.* **2021**, *21*, 2997−3006.

(16) Cote, A. P.; Benin, A. I.; Ockwig, N. W.; O'Keeffe, M.; Matzger, A. J.; Yaghi, O. M. Porous, crystalline, covalent organic frameworks. *Science* **2005**, *310*, 1166−1170.

(17) Ma, T. Q.; Kapustin, E. A.; Yin, S. X.; Liang, L.; Zhou, Z. Y.; Niu, J.; Li, L. H.; Wang, Y. Y.; Su, J.; Li, J.; Wang, X. G.; Wang, W. D.; Wang, W.; Sun, J. L.; Yaghi, O. M. Single-crystal x-ray diffraction structures of covalent organic frameworks. *Science* **2018**, *361*, 48−52.

(18) Fan, H.; Peng, M.; Strauss, I.; Mundstock, A.; Meng, H.; Caro, J. High-flux vertically aligned 2D covalent organic framework membrane with enhanced hydrogen separation. *J. Am. Chem. Soc.* **2020**, *142*, 6872−6877.

(19) Zhang, P.; Chen, S.; Zhu, C.; Hou, L.; Xian, W.; Zuo, X.; Zhang, Q.; Zhang, L.; Ma, S.; Sun, Q. Covalent organic framework nanofluidic membrane as a platform for highly sensitive bionic thermosensation. *Nat. Commun.* **2021**, *12*, 1844.

(20) Jiang, S. Y.; Gan, S. X.; Zhang, X.; Li, H.; Qi, Q. Y.; Cui, F. Z.; Lu, J.; Zhao, X. Aminal-linked covalent organic frameworks through condensation of secondary amine with aldehyde. *J. Am. Chem. Soc.* **2019**, *141*, 14981−14986.

(21) He, X.; Yang, Y.; Wu, H.; He, G.; Xu, Z.; Kong, Y.; Cao, L.; Shi, B.; Zhang, Z.; Tongsh, C.; Jiao, K.; Zhu, K.; Jiang, Z. *De Novo* design of covalent organic framework membranes toward ultrafast anion transport. *Adv. Mater.* **2020**, *32*, 2001284.

(22) Zhu, D.; Xu, G.; Barnes, M.; Li, Y.; Tseng, C. P.; Zhang, Z.; Zhang, J. J.; Zhu, Y.; Khalil, S.; Rahman, M. M.; Verduzco, R.; Ajayan, P. M. Covalent organic frameworks for batteries. *Adv. Funct. Mater.* **2021**, *31*, 2100505.

(23) Geng, K.; He, T.; Liu, R.; Dalapati, S.; Tan, K. T.; Li, Z.; Tao, S.; Gong, Y.; Jiang, Q.; Jiang, D. Covalent organic frameworks: design, synthesis, and functions. *Chem. Rev.* **2020**, *120*, 8814−8933.

(24) Sasmal, H. S.; Halder, A.; Kunjattu, H. S.; Dey, K.; Nadol, A.; Ajithkumar, T. G.; Ravindra Bedadur, P.; Banerjee, R. Covalent self-assembly in two dimensions: connecting covalent organic framework nanospheres into crystalline and porous thin films. *J. Am. Chem. Soc.* **2019**, *141*, 20371−20379.

(25) Li, Z.; He, T.; Gong, Y.; Jiang, D. Covalent organic frameworks: pore design and interface engineering. *Acc. Chem. Res.* **2020**, *53*, 1672−1685.

(26) Lohse, M. S.; Bein, T. Covalent organic frameworks: structures, synthesis, and applications. *Adv. Funct. Mater.* **2018**, *28*, 1705553.

(27) Yang, Y.; Zhang, P.; Hao, L.; Cheng, P.; Chen, Y.; Zhang, Z. Grotthuss proton-conductive covalent organic frameworks for efficient proton pseudocapacitors. *Angew. Chem., Int. Ed.* **2021**, *60*, 21838−21845.

(28) Kandambeth, S.; Dey, K.; Banerjee, R. Covalent organic frameworks: chemistry beyond the structure. *J. Am. Chem. Soc.* **2019**, *141*, 1807−1822.

(29) Guo, C.; Liu, M.; Gao, G. K.; Tian, X.; Zhou, J.; Dong, L. Z.; Li, Q.; Chen, Y.; Li, S. L.; Lan, Y. Q. Anthraquinone covalent organic framework hollow tubes as binder microadditives in Li−S batteries. *Angew. Chem., Int. Ed.* **2021**, *60*, 2−11.

(30) Vitaku, E.; Gannett, C. N.; Carpenter, K. L.; Shen, L.; Abruna, H. D.; Dichtel, W. R. Phenazine-based covalent organic framework cathode materials with high energy and power densities. *J. Am. Chem. Soc.* **2020**, *142*, 16−20.

(31) Lu, Y.; Chen, J. Prospects of organic electrode materials for practical lithium batteries. *Nat. Rev. Chem.* **2020**, *4*, 127−142.

(32) Luo, C.; Xu, G. L.; Ji, X.; Hou, S.; Chen, L.; Wang, F.; Jiang, J.; Chen, Z.; Ren, Y.; Amine, K.; Wang, C. Reversible redox chemistry of

azo compounds for sodium-ion batteries. *Angew. Chem., Int. Ed.* **2018**, *57*, 2879−2883.
(33) Luo, C.; Borodin, O.; Ji, X.; Hou, S.; Gaskell, K. J.; Fan, X.; Chen, J.; Deng, T.; Wang, R.; Jiang, J.; Wang, C. Azo compounds as a family of organic electrode materials for alkali-ion batteries. *Proc. Natl. Acad. Sci. U.S.A.* **2018**, *115*, 2004−2009.
(34) Uribe-Romo, F. J.; Doonan, C. J.; Furukawa, H.; Oisaki, K.; Yaghi, O. M. Crystalline covalent organic frameworks with hydrazone linkages. *J. Am. Chem. Soc.* **2011**, *133*, 11478−81.
(35) Tang, W.; Aslam, M. K.; Xu, M. Towards high performance room temperature sodium-sulfur batteries: strategies to avoid shuttle effect. *J. Colloid Interface Sci.* **2022**, *606*, 22−37.
(36) Xu, F.; Wang, Y.; Lian, C.; Xu, Z. Fast proton-selective transport through covalent organic frameworks in aqueous phase. *J. Membr. Sci.* **2022**, *648*, 120361.
(37) Pei, F.; Lin, L.; Fu, A.; Mo, S.; Ou, D.; Fang, X.; Zheng, N. A two-dimensional porous carbon-modified separator for high-energy-density Li-S batteries. *Joule* **2018**, *2*, 323−336.
(38) Li, Y.; Gao, T.; Ni, D.; Zhou, Y.; Yousaf, M.; Guo, Z.; Zhou, J.; Zhou, P.; Wang, Q.; Guo, S. Two birds with one stone: interfacial engineering of multifunctional janus separator for lithium−sulfur batteries. *Adv. Mater.* **2021**, 2107638.
(39) Wu, C.; Hu, M.; Yan, X.; Shan, G.; Liu, J.; Yang, J. Azo-linked covalent triazine-based framework as organic cathodes for ultrastable capacitor-type lithium-ion batteries. *Energy Stor. Mater.* **2021**, *36*, 347−354.
(40) Fan, H.; Mundstock, A.; Feldhoff, A.; Knebel, A.; Gu, J.; Meng, H.; Caro, J. Covalent organic framework-covalent organic framework bilayer membranes for highly selective gas separation. *J. Am. Chem. Soc.* **2018**, *140*, 10094−10098.
(41) Guo, Q.; Sun, S.; Kim, K. i.; Zhang, H.; Liu, X.; Yan, C.; Xia, H. A novel one-step reaction sodium-sulfur battery with high areal sulfur loading on hierarchical porous carbon fiber. *Carbon Energy* **2021**, *3*, 440−448.
(42) Xiao, F.; Wang, H.; Yao, T.; Zhao, X.; Yang, X.; Yu, D. Y. W.; Rogach, A. L. MOF-derived $CoS_2$/N-doped carbon composite to induce short-chain sulfur molecule generation for enhanced sodium-sulfur battery performance. *ACS Appl. Mater. Interfaces* **2021**, *13*, 18010−18020.
(43) Kang, N.; Lin, Y.; Yang, L.; Lu, D.; Xiao, J.; Qi, Y.; Cai, M. Cathode porosity is a missing key parameter to optimize lithium-sulfur battery energy density. *Nat. Commun.* **2019**, *10*, 4579.
(44) Klein, J.; Beerhues, J.; Schweinfurth, D.; van der Meer, M.; Gazvoda, M.; Lahiri, G. K.; Kosmrlj, J.; Sarkar, B. Versatile coordination of azocarboxamides: redox-triggered change of the chelating binding pocket in ruthenium complexes. *Chem.-Eur. J.* **2018**, *24*, 18020−18031.
(45) Cao, Y.; Liu, C.; Wang, M.; Yang, H.; Liu, S.; Wang, H.; Yang, Z.; Pan, F.; Jiang, Z.; Sun, J. Lithiation of covalent organic framework nanosheets facilitating lithium-ion transport in lithium-sulfur batteries. *Energy Stor. Mater.* **2020**, *29*, 207−215.





https://doi.org/10.1021/acsnano.2c04273
*ACS Nano* 2022, 16, 14178−14187